SCIENCE CHINA
Chemistry

•ARTICLES•

June 2023 Vol.66 No.6: 1834–1843
https://doi.org/10.1007/s11426-023-1591-6

Operando reconstruction towards stable CuI nanodots with favorable facets for selective CO_2 electroreduction to C_2H_4

Wenjie Xue[1], Hongxia Liu[2], Xinqing Chen[3], Xiaoju Yang[1], Ruoou Yang[4], Youwen Liu[4], Minghao Li[1], Xuan Yang[1*], Bao Yu Xia[1*] & Bo You[1*]

[1]*Key Laboratory of Material Chemistry for Energy Conversion and Storage, Ministry of Education, Hubei Key Laboratory of Material Chemistry and Service Failure, School of Chemistry and Chemical Engineering, Huazhong University of Science and Technology, Wuhan 430074, China;*
[2]*School of Chemistry and Chemical Engineering, Wuhan Textile University, Wuhan 430200, China;*
[3]*Shanghai Advanced Research Institute, Chinese Academy of Sciences, Shanghai 201210, China;*
[4]*State Key Laboratory of Materials Processing and Die & Mold Technology, and School of Materials Science and Engineering Huazhong University of Science and Technology, Wuhan 430074, China*

Received February 6, 2023; accepted April 10, 2023; published online April 24, 2023

Cu-based electrocatalysts with favorable facets and Cu^+ can boost CO_2 reduction to valuable multicarbon products. However, the inevitable Cu^+ reduction and the phase evolution usually result in poor performance. Herein, we fabricate CuI nanodots with favorable (220) facets and a stable Cu^+ state, accomplished by *operando* reconstruction of $Cu(OH)_2$ under CO_2- and I^--containing electrolytes for enhanced CO_2-to-C_2H_4 conversion. Synchrotron X-ray absorption spectroscopy (XAS), *in-situ* Raman spectroscopy and thermodynamic potential analysis reveal the preferred formation of CuI. Vacuum gas electroresponse and density functional theory (DFT) calculations reveal that CO_2-related species induce the exposure of the (220) plane of CuI. Moreover, the small size of nanodots enables the adequate contact with I^-, which guarantees the rapid formation of CuI instead of the electroreduction to Cu^0. As a result, the resulting catalysts exhibit a high C_2H_4 Faradaic efficiency of 72.4% at a large current density of 800 mA cm^{-2} and robust stability for 12 h in a flow cell. Combined *in-situ* ATR-SEIRS spectroscopic characterizations and DFT calculations indicate that the (220) facets and stable Cu^+ in CuI nanodots synergistically facilitate CO_2/*CO adsorption and *CO dimerization.

CO_2 reduction reaction, cuprous iodide, favorable facets, halogen electrolyte, reconstruction

Citation: Xue W, Liu H, Chen X, Yang X, Yang R, Liu Y, Li M, Yang X, Xia BY, You B. *Operando* reconstruction towards stable CuI nanodots with favorable facets for selective CO_2 electroreduction to C_2H_4. *Sci China Chem*, 2023, 66: 1834–1843, https://doi.org/10.1007/s11426-023-1591-6

1 Introduction

In the context of carbon neutralization, renewable energy-driven electroreduction of CO_2 (CO_2R) to valuable energy-dense C_{2+} hydrocarbons and oxygenates (*e.g.*, C_2H_4, C_2H_5OH, C_3H_7OH) beyond CO or HCOOH represents an intriguing approach to address our current energy and climate challenges [1–4]. Among all the products, C_2H_4 is of most economic value in view of its vital role in modern chemical industry [5–7]. Copper is the only metal that can reduce CO_2 to produce C_2H_4, while the bulk Cu electrode normally exhibits high overpotentials and poor selectivity [8–10]. Up to now, various strategies have been reported to tailor the particle size, shape, composition and oxidation state of Cu-based electrocatalysts for efficient and selective C_2H_4 production [11–16]. For example, oxide-derived copper (OD-Cu) exhibits the enhanced selectivity towards C_2H_4, which

*Corresponding authors (email: xuanyang@hust.edu.cn; byxia@hust.edu.cn; youbo@hust.edu.cn)

was later partly explained by the existence of Cu^+ species *via* theoretical and *operando* spectroscopy studies [17]. Besides, faceting Cu with (100) plane exposure favors C_2 over C_1 production, contrary to the Cu(111) facets [18]. Recent studies have showed that electrodeposited Cu under CO_2R conditions prefers the exposure of (100) facets due to the capping roles of intermediates along reductive pathways [19]. It is believed that both Cu^+ and Cu(100) facets in Cu-based electrocatalysts can optimize the adsorption of *CO intermediates to improve the *CO dimerization for C_{2+} production [20–24]. Unfortunately, the Cu^+ inevitably undergoes the electroreduction to Cu^0 during the CO_2R process even if a variety of innovative stabilization approaches, such as secondary metal/heteroatom doping, plasma treating, and matrix incorporating, are employed [25–28]. Concomitantly, the morphology reconstruction of catalysts usually leads to dynamically active sites and/or deteriorated C_{2+} selectivity as well as complicates their structure–activity correlation [29–33]. It is still challenging to explore advanced Cu-based electrocatalysts with both favorable facets and stable Cu^+ states for the selective CO_2-to-C_2H_4 conversion.

Different from previous reports that focused on metallic/oxidized Cu, we herein fabricate cuprous iodide (CuI) nanodots (diameter of 5.3 nm) with favorable (220) facets and stable Cu^+ states for improved CO_2-to-C_{2+} (C_2H_4) conversion through the *operando* reconstruction of $Cu(OH)_2$ precursors under CO_2- and I^--containing electrolytes. The high thermodynamic potential of Cu^{2+}/CuI relative to Cu^{2+}/Cu^+(Cu^0) benefits the formation of stable CuI rather than metallic Cu during the CO_2R process, as revealed by the X-ray absorption spectroscopy and *in-situ* Raman spectroscopy investigations. CO_2-related intermediates along reductive pathways serve as capping agents to shape the formation of CuI(220). The adequate contact of nanodots with I^- due to the small size guarantees the rapid formation of CuI rather than the electroreduction to Cu^0. As a result, we achieve a high C_2H_4 Faradaic efficiency (FE) of 72.4% at 800 mA cm^{-2} and long-term stability for the resulting CuI nanodots. *In-situ* attenuated total reflection surface-enhanced Fourier-transform infrared spectroscopy (ATR-SEIRS) and density functional theory results indicate the high-index CuI (220) facets and stable Cu^+ collectively facilitate CO_2/*CO adsorption and subsequent *CO dimerization for improved C_2H_4 generation.

2 Results and discussion

2.1 Catalyst synthesis and characterizations

The *operando* reconstruction synthesis of CuI nanodots with high-index facets and a stable Cu^+ state was achieved by the electroreduction of carbon paper-supported copper hydroxide ($Cu(OH)_2$) precursors in CO_2-saturated 0.1 mol L^{-1} $KHCO_3$/KI solution (labeled as CuI–CO_2). Two control samples named CuI–N_2 and Cu–CO_2 were also prepared under similar conditions for the comparison by replacing CO_2 gas with N_2 gas and removing KI, respectively. Additional details on the synthesis parameters are shown in the Supporting Information. The typical X-ray diffraction (XRD) patterns of the CuI–CO_2, CuI–N_2 and Cu–CO_2 electrocatalysts are shown in Figure 1a. Three pronounced diffraction peaks for both CuI–CO_2 and CuI–N_2 at 2θ=25.5°, 42.2° and 50.0° corresponded to the (111), (220) and (311) planes of standard CuI (PDF 06-0246), suggesting the successful transformation to CuI from $Cu(OH)_2$ (Figure S1). By contrast, metallic Cu^0 can be obtained for Cu–CO_2 without iodide ions (I^-), highlighting its role in promoting the CuI formation, which is obviously different from previous reports [31–33]. Notably, the relative peak intensity of (220)/(111) for CuI–CO_2 ($R_{(220)/(111)}$=1.30) is much higher than that of CuI–N_2 ($R_{(220)/(111)}$=0.91), implying that CO_2-related species favor the exposure of (220) facets. To further investigate the chemical states of CuI–CO_2, CuI–N_2 and Cu–CO_2, X-ray photoelectron spectroscopy (XPS) was then used (Figure 1b, c and Figure S2). The high-resolution Cu 2p XPS spectra for all three electrocatalysts show double peaks at binding energies of 932.6 and 952.4 eV assignable to Cu $2p_{3/2}$ and Cu $2p_{1/2}$ of either Cu^+ or Cu^0, respectively (Figure S2), suggesting the complete reduction of $Cu(OH)_2$. Since the Cu 2p peaks for Cu^+ and Cu^0 are too close to be separated, the Cu LMM Auger spectra were then collected to distinguish Cu^+ from Cu^0. As shown in Figure 1b, a pronounced peak at 570.5 eV attributed to Cu^+ species can be observed for both CuI–CO_2 and CuI–N_2, in sharp contrast to that at 568.4 eV assigned to Cu^0 species for Cu–CO_2 [32]. Moreover, the high-resolution I 3d XPS spectra (Figure 1c) reveal the presence of I^- at 619.7 eV in both CuI–CO_2 and CuI–N_2, which is missing in Cu–CO_2. High-magnification transmission (TEM) and scanning electron microscopy (SEM) reveal a dot-like morphology of CuI–CO_2 with a mean diameter of 5.3 nm and a homogeneous distribution in the carbon matrix (Figure 1d and Figure S3), analogous to those of pristine Cu $(OH)_2$ (Figure S4). A closer inspection of these nanodots in a high-resolution TEM (HR-TEM) image indicates the (220) plane of CuI with a lattice fringe of 0.214 nm (Figure 1e), in accordance with the XRD and XPS results. Scanning TEM and the corresponding elemental mapping images demonstrate that both Cu and I, along with C, are uniformly distributed throughout the whole sample of CuI–CO_2, strongly verifying the successful chemical conversion of $Cu(OH)_2$ to CuI and the uniform spatial distribution on the carbon matrix *via* our *operando* reconstruction process.

We further employed synchrotron X-ray absorption spectroscopy (XAS) to investigate the atomic structure of CuI–CO_2 nanodots. The results given in Figure 2a show the comparison of the Cu *K*-edge spectra of CuI–CO_2 with those

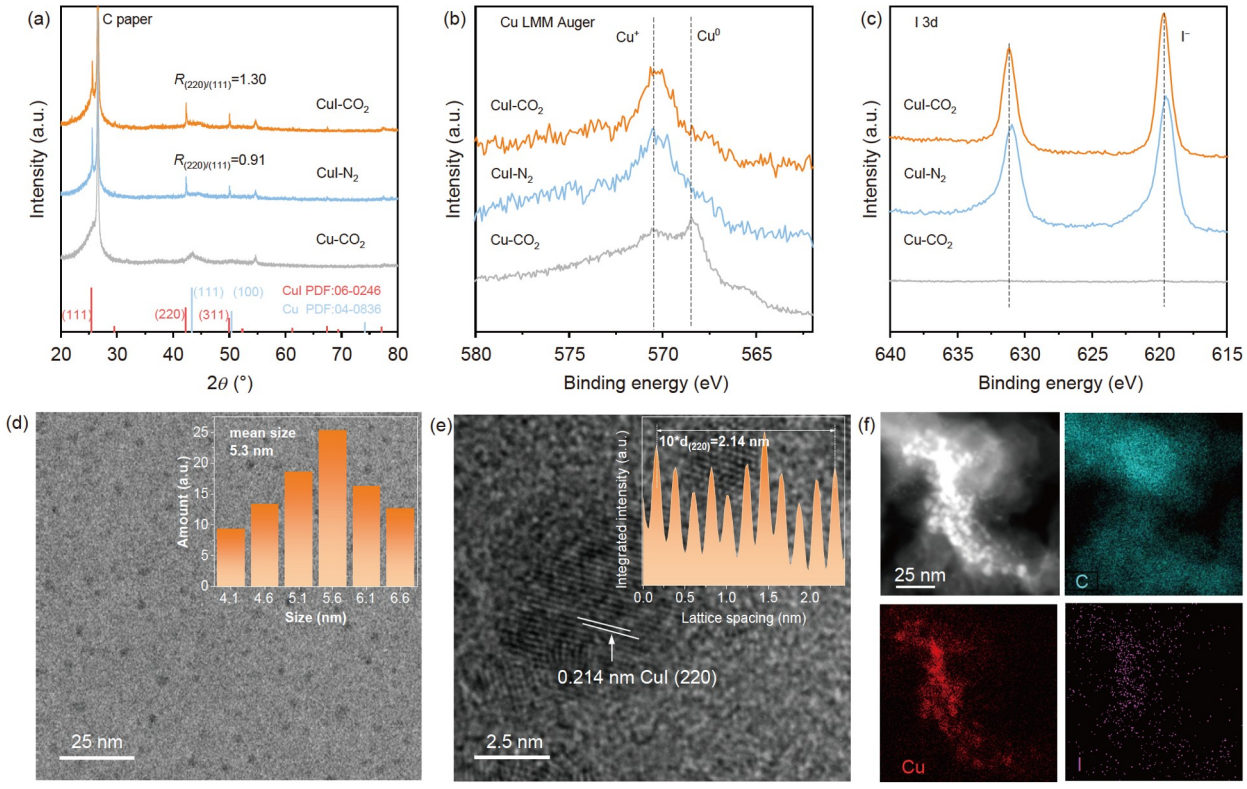

Figure 1 Morphology and structure characterizations. (a) XRD patterns of CuI–CO_2, CuI–N_2 and Cu–CO_2 electrocatalysts. (b, c) Cu LMM Auger and I 3d XPS spectra. (d) TEM image and the corresponding size distribution of CuI for CuI–CO_2 catalysts. (e) HR-TEM images of CuI–CO_2 catalysts. (f) STEM and the corresponding elemental mapping images of CuI–CO_2 (color online).

of the reference samples, indicating that the oxidation states of Cu in CuI–CO_2 lie between 0 and +2, which is in accordance with the XPS results. The Fourier transform extended X-ray absorption fine structure (FT-EXAFS) spectra (Figure 2b) of CuI–CO_2 shows a dominant peak at 2.40 Å derived from the shell coordination of Cu–I, which is different from those of Cu–Cu and Cu–O. In addition, the FT-EXAFS spectrum analyzed by fitting shows an average shell coordination number of 4 and a bond length of 2.50 Å for Cu–I, coinciding with CuI (Figure 2c and Table S1). The wavelet-transform extended X-ray absorption fine structures (WT-EXAFS) were also analyzed to examine the coordination of CuI–CO_2 (Figure 2d–f). The wavelet transform signal from CuI–CO_2 in the *k* range from 3 $Å^{-1}$ to 10 $Å^{-1}$ is different from those for the Cu foil and CuO reference, which is attributed to the Cu–I coordination. Collectively, these characterizations unambiguously validate the successful synthesis of CuI nanodots with preferred (220) facets and Cu^+ states.

2.2 Synthetic mechanism of CuI–CO_2 nanodots

The critical roles of I^- and CO_2-related species in CuI–CO_2 were further scrutinized by the thermodynamic potential analysis/*in-situ* Raman spectroscopy and vacuum gas adsorption/theory calculations, respectively. To explain the electroreduction of Cu^{2+} from $Cu(OH)_2$ to CuI instead of metallic Cu (Figure 3a), thermodynamic potential analysis of Cu^{2+}/Cu^0, Cu^{2+}/Cu^+ and Cu^{2+}/CuI pairs was conducted first [34]. As depicted in Figure 3b, the higher thermodynamic potential of Cu^{2+}/Cu^0 (0.34 V) than that of Cu^{2+}/Cu^+ (0.16 V) suggests the easier reduction of Cu^{2+} to Cu^0 rather than Cu^+, aligning with the experimental phenomenon reported in numerous studies [17,22–24,28,29]. Remarkably, the Cu^{2+}/CuI pair possesses the highest thermodynamic potential (0.86 V), indicative of the easiest formation of CuI from Cu^{2+} reduction.

Subsequently, we performed *in-situ* Raman spectroscopy to track the conversion course from Cu^{2+} to CuI (Figure 3c, d). Figure 3c shows the Raman spectra evolution of pristine $Cu(OH)_2$ in the electrolyte with and without I^- over the cathodic electroreduction time. The characteristic Raman band at 274.8 cm^{-1} corresponding to $Cu(OH)_2$ rapidly disappears during the cathodic electroreduction regardless of whether there is I^- in the electrolyte, suggesting the quick reduction of $Cu(OH)_2$. Specifically, in the I^--containing electrolyte, two new peaks at 73.9 and 105.8 cm^{-1} ascribed to CuI gradually appear as the electroreduction time increases from 100 to 900 s (Figure 3d) [35], different from that without I^- wherein no new peaks emerge. These *in-situ* Ra-

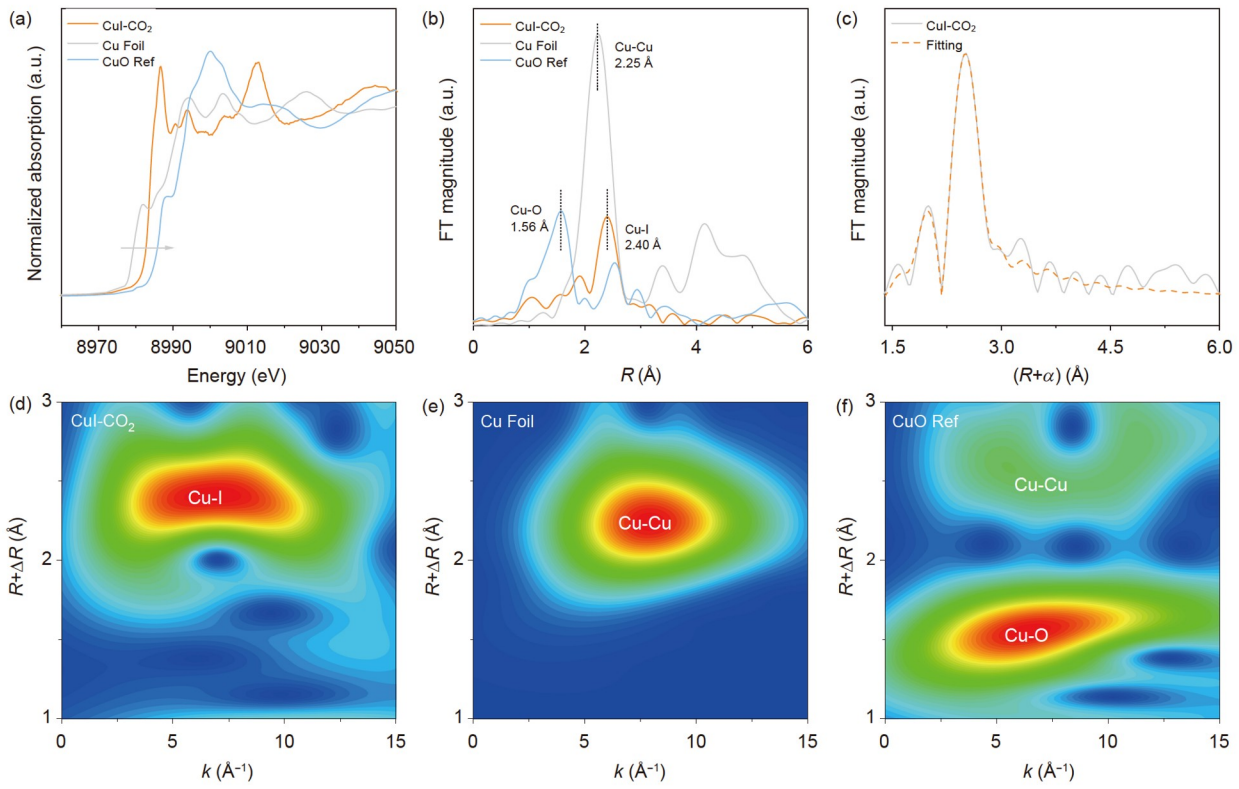

Figure 2 XAS spectroscopy characterizations. (a) Cu *K*-edge XANES spectra. (b) FT k^2-weighted EXAFS spectra. (c) Fitting curve of the FT-EXAFS spectrum. The data are k^2-weighted and not phase-corrected and (d–f) wavelet transform EXAFS of CuI–CO_2, Cu foil and CuO reference (color online).

man spectroscopy characterizations further confirm the chemical conversion from $Cu(OH)_2$ to CuI in the electrolyte with I^-, in agreement with the XRD, TEM and XPS results (Figure 1).

Previous research has shown that CO_2 and the intermediates along reductive pathways can function as capping agents to specifically adsorb on a crystal plane of metals such as Cu and Pb to promote their exposure and thus shape the facets [4,19]. We speculated that this similar effect may be applied to steer the surface reconstruction of CuI nanodots. In this respect, the adsorption energies of key species involved in CO_2R (Figure S5) and the hydrogen evolution reaction (HER) on Cu(111), CuI(111), CuI(220) and CuI (311) facets were calculated based on density functional theory (DFT). As shown in Figure 3e, the adsorption energies for both CO_2 and *CO intermediates over Cu and CuI are negatively higher than those of *H intermediates related to the HER, presaging their preferred adsorption of CO_2 and *CO relative to *H. In particular, all three facets of CuI, including (111), (220) and (311), demonstrate more negative adsorption energies for both CO_2 and *CO intermediates compared with those for Cu(111) facets, indicating stronger adsorption over the CuI facets. Among them, the CuI(220) facets present the most negative adsorption energies for CO_2 and *CO, evidencing that both CO_2 and *CO favor the exposure of CuI(220) facets, which is in line with the XRD results (Figure 1a). To experimentally support the DFT calculations, we also conducted vacuum CO gas adsorption electroresponse testing over the three electrocatalysts (Figure 3f). The results disclose that CO adsorption responses over CuI–CO_2 with favorable (220) facets are stronger than those of CuI–N_2 and Cu–CO_2, implying the enhanced adsorption and activation of CO.

2.3 Electrochemical CO_2 reduction in an H-cell

To examine the positive roles of favorable (220) facets and stable Cu^+ on improved CO_2 reduction to C_2H_4, we performed electrocatalytic measurements in a conventional H-cell using CuI–CO_2, CuI–N_2 and Cu–CO_2 as electrocatalysts. The reduction products under different potentials were detected and analyzed through on-line gas chromatography (GC) and off-line ^1H NMR (Figure S6). As shown in Figure 4a–c, the product distributions of CO_2R over the three electrocatalysts are C_2H_5OH, C_2H_4, HCOOH, CO and CH_4 as well as H_2 from HER with a total FE of almost 100% (Table S2-4). Remarkably, the CuI–CO_2 nanodots achieve a high C_2H_4 FE of 45.3% at −1.2 V *vs*. reversible hydrogen electrode (RHE) without *iR* compensation (Figure 4a), substantially higher than Cu–CO_2 (20.5%) at the same potential (Figure 4d). After *iR* correction, the potential at the highest C_2H_4 FE for CuI–CO_2 nanodots is only −0.92 V *vs*. RHE

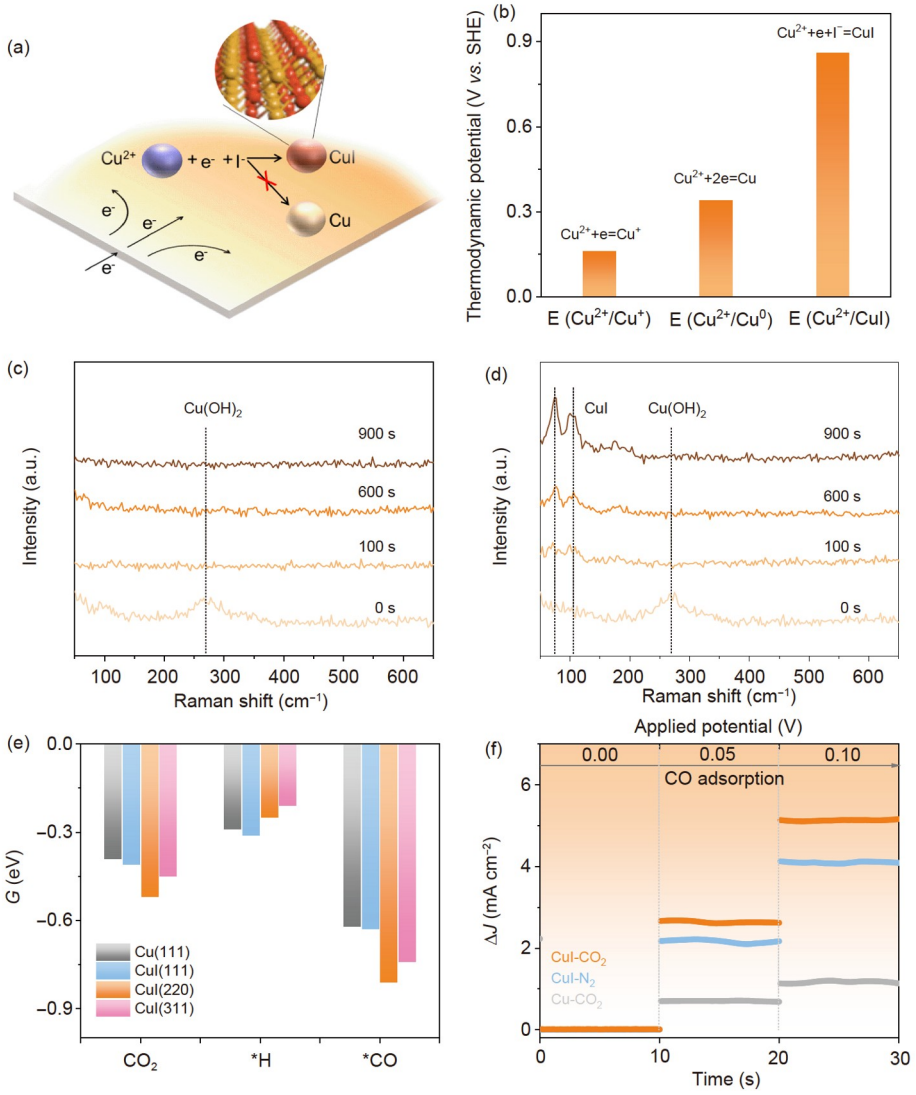

Figure 3 Catalyst synthesis mechanism investigations. (a) Schematic diagram of the reduction of Cu^{2+} to CuI. (b) The thermodynamic potentials of the different reactions. (c, d) *In-situ* Raman spectra of $Cu(OH)_2$ in the CO_2-saturated 0.2 mol L^{-1} $KHCO_3$ and 0.1 mol L^{-1} $KHCO_3$/KI solutions at −1.2 V *vs.* RHE. (e) The adsorption energy of key species during CO_2R on Cu(111), CuI(111), CuI(220), and CuI(311) facets. (f) Vacuum CO adsorption electro-responses under different applied voltages for the CuI–CO_2, CuI–N_2 and Cu–CO_2 electrocatalysts (color online).

(Figure S7), which is more positive than those of CuI–N_2 (−0.96 V *vs.* RHE) and Cu–CO_2 (−0.97 V *vs.* RHE). These results undoubtedly underscore that CuI with stable Cu^+ induced by I^- is beneficial for improved C_2H_4 selectivity. To explore the importance of the (220) facets, the CO_2R performance of another control sample, CuI–N_2 with less (220) facet exposure, was investigated for comparison (Figure 4b). The C_2H_4 FE of CuI–N_2 is only 35.6% at −1.2 V *vs.* RHE, which is lower than that of the CuI–CO_2 catalyst, highlighting the positive contribution of the (220) facets to enhanced C_2H_4 production. In fact, under all investigated potentials, our CuI–CO_2 nanodots exhibit the highest C_2H_4 FE compared to the CuI–N_2 and Cu–CO_2 controls (Figure 4d). To better evaluate the intrinsic activities of CuI–CO_2, CuI–N_2 and Cu–CO_2, their apparent current densities for C_2H_4 generation were normalized to electrochemically active surface areas (ECSAs), which were determined by collecting cyclic voltammograms in a non-Faradaic region under different scan rates (Figure S8). As plotted in Figure S8d, the linear slope of CuI–CO_2 (4.5 mF cm^{-2}) is slightly higher than those of CuI–N_2 (4.0 mF cm^{-2}) and Cu–CO_2 (4.2 mF cm^{-2}), indicating the larger ECSA of the former. With their contact resistances and ECSAs in hand, the ECSA-normalized current densities of the C_2H_4-potential curves can be obtained (Figure 4e). It is clear that the CuI–CO_2 nanodots show much better intrinsic CO_2R activity for C_2H_4 production than either CuI–N_2 or Cu–CO_2. Considering their similar particle sizes (Figure 1d and Figure S9), we believe that the superior CO_2-to-C_2H_4 activity of CuI–CO_2 can be ascribed to the favorable (220) facets and stable Cu^+ state.

The stability of the CuI–CO_2 nanodots in an H-cell was also examined by the chronoamperometry for CO_2 electrolysis at a constant potential of −1.2 V *vs*. RHE. The experimental results in Figure 4f demonstrate only a slight decrease in current density and a small loss of C_2H_4 selectivity over 20 h, even with repeated occasional refreshing of the electrolyte. The robust long-term stability of CuI–CO_2 nanodots for C_2H_4 generation from CO_2R originates from the stable Cu^+ species and favorable facets, which was corroborated by the following XPD, XPS and TEM characterizations of the CuI–CO_2 nanodots during stability testing.

Ex-situ XRD pattern was first conducted to examine the crystal structure of CuI–CO_2 nanodots after 20 h of electrolysis (denoted CuI–CO_2-20) (Figure 5a). The XRD pattern for the CuI–CO_2-20 electrocatalysts clearly displays the maintenance of CuI, and the peaks attributed to metallic Cu are lacking even after 20 h of electrolysis. Moreover, the almost constant ratios of the relative peak intensity of the (220)/(111) facets for CuI–CO_2-20 across the time course further verify the superior stability of CuI–CO_2 nanodots. The Cu LMM Auger (Figure 5b) and I 3d XPS spectra (Figure S10) of CuI–CO_2-20 evidently reveal that the peak at

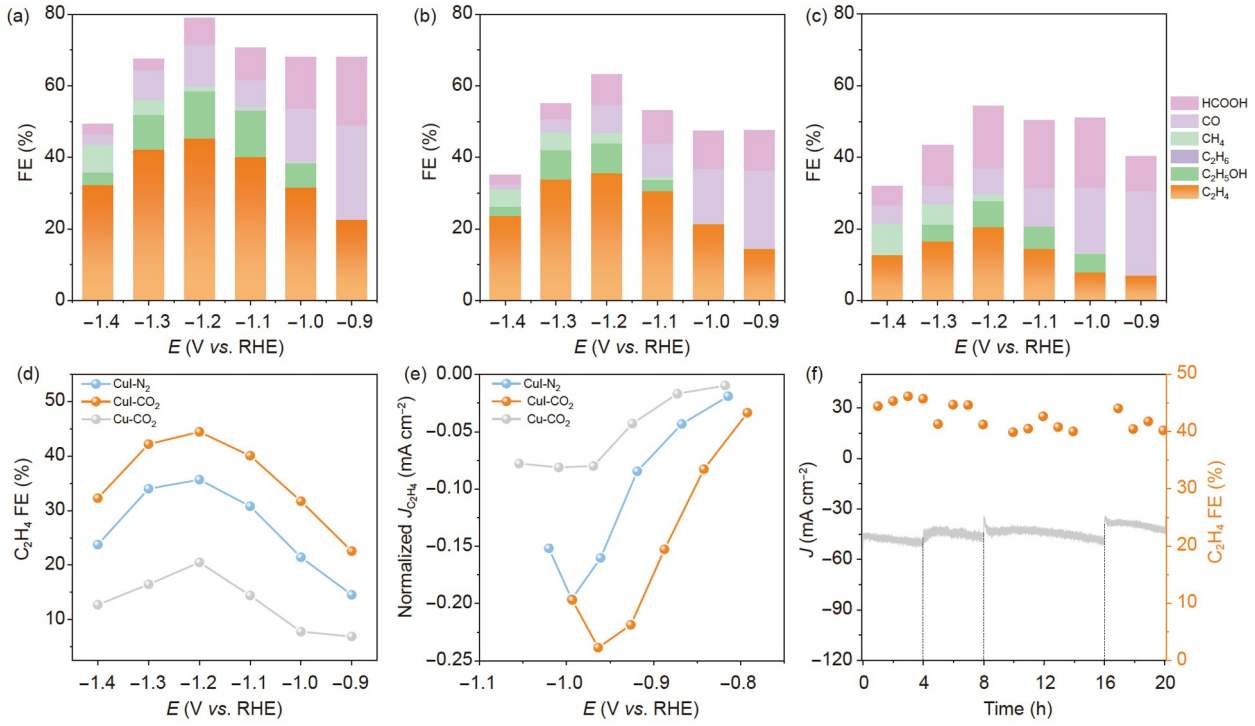

Figure 4 CO_2R performance in an H-cell. (a–c) The main product distributions at various potentials ranging from −0.9 to −1.4 V *vs*. RHE in 0.1 mol L^{-1} $KHCO_3$/KI solutions over CuI–CO_2, CuI–N_2 and Cu–CO_2 electrocatalysts without *iR* correction. (d) The FEs of C_2H_4 products under different potentials over the three electrocatalysts. (e) ECSA-normalized current densities of C_2H_4 products over different electrocatalysts in CO_2-saturated electrolytes with *iR* correction. (f) CO_2R stability test of CuI–CO_2 over 20 h in 0.1 mol L^{-1} $KHCO_3$/KI at −1.2 V *vs*. RHE (color online).

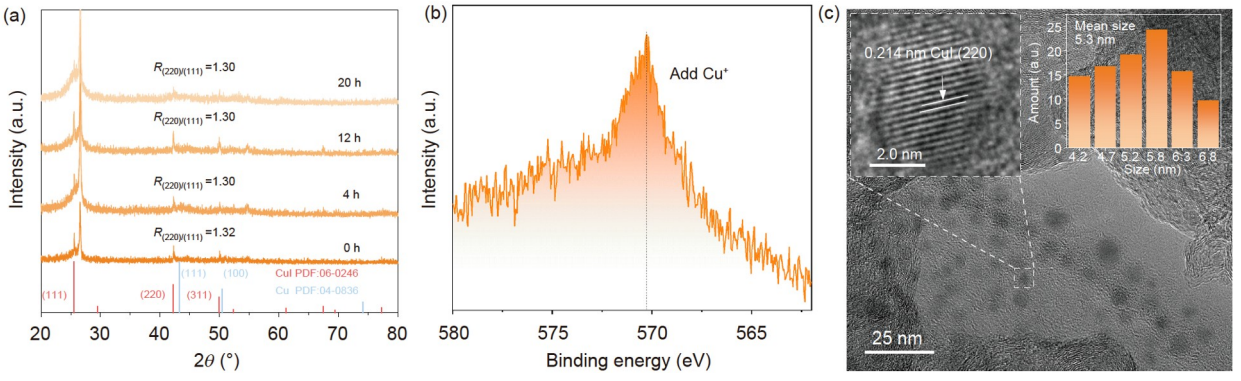

Figure 5 Morphology and structure characterizations of the CuI–CO_2 catalyst after stability testing in an H-cell. (a) XRD patterns, (b) Cu LMM Auger spectra, (c) TEM and HR-TEM images with the corresponding particle size distribution of CuI (color online).

570.3 eV attributed to Cu^+ and the peak ascribed to I species can be easily observed, which undoubtedly substantiates that Cu^+ can be stabilized by I^- ions. The high-magnification TEM image of CuI–CO_2-20 (Figure 5c) exhibits a uniform distribution of CuI nanodots with a mean diameter of 5.3 nm, similar to that of fresh CuI–CO_2 (Figure 1d). In addition, the HR-TEM image indicates an interlayer spacing of 0.214 nm, corresponding to the (220) planes of CuI.

To explore the origin of the robust stability of our CuI–CO_2 nanodots, another two control samples, commercial CuI with a size of approximately 300 nm and thermally synthesized CuI with a size of approximately 1,500 nm, were subjected to similar CO_2R tests (Figure S11 and Table S5, S6). XRD patterns of the thermally synthesized CuI show that the characteristic peak of CuI(111) disappeared at −1.2 V *vs.* RHE in 0.1 mol L^{-1} $KHCO_3$/KI solutions after 2 h of electrolysis, and the characteristic peak of Cu appeared after 8 h of electrolysis (Figure S12), indicating its electroreduction to Cu^0. Similarly, the XRD patterns of commercial CuI show that the peak of CuI(111) is gradually weakened after 4 h of electrolysis and almost disappears after 8 h of electrolysis. Both are worse than our CuI–CO_2 nanodots, and the stability of the three catalysts is in the order of CuI–CO_2 > commercial CuI > thermal synthesis CuI, opposite to their size order of 5.3 nm<300 nm<1,500 nm. We thus preliminarily anticipate that the superior stability of CuI–CO_2 nanodots is ascribed to the ultrasmall particle size (large surface area), which ensures adequate contact with I^- in the electrolyte for the rapid formation of CuI instead of the electroreduction to Cu^0. Certainly, more detailed studies are needed in the future. The excellent stability and performance of CuI–CO_2 nanodots encouraged us to further explore their CO_2R performance in a flow cell at high current densities.

2.4 Electrochemical CO_2 reduction in a flow cell

Flow cells have been recently reported to substantially promote the rate of CO_2R (>200 mA cm^{-2}) by taking advantage of the excellent diffusion of CO_2 in these reactors. The CO_2R performance of the CuI–CO_2 nanodots was therefore evaluated in a flow cell with an electrode area of 1 cm^{-2} using 0.5 mol L^{-1} $KHCO_3$/KI solution as the electrolyte. Figure 6a shows the partial current density for C_2H_4 products under different potentials without *iR* correction. The CuI–CO_2 nanodots show a high C_2H_4 partial current density of 688 mA cm^{-2} at approximately −2.2 V *vs.* RHE (Figure 6a). Figure 6b and Table S7 show the FEs for C_2H_4 and other products at various current densities ranging from 400–1,000 mA cm^{-2}. As the consumption of CO_2 due to the dissolution in the electrolyte will lead to the overestimation of FEs, we consider the real outlet flow rate of CO_2 for the FE calculations (Figure S13) [36,37]. It can be observed that CuI–CO_2 achieves a remarkable C_2H_4 FE of 72.4% with a current density of 800 mA cm^{-2}. It is worth noting that such a high C_2H_4 FE with a large current density is superior to those of many reported Cu-based CO_2R electrocatalysts in flow

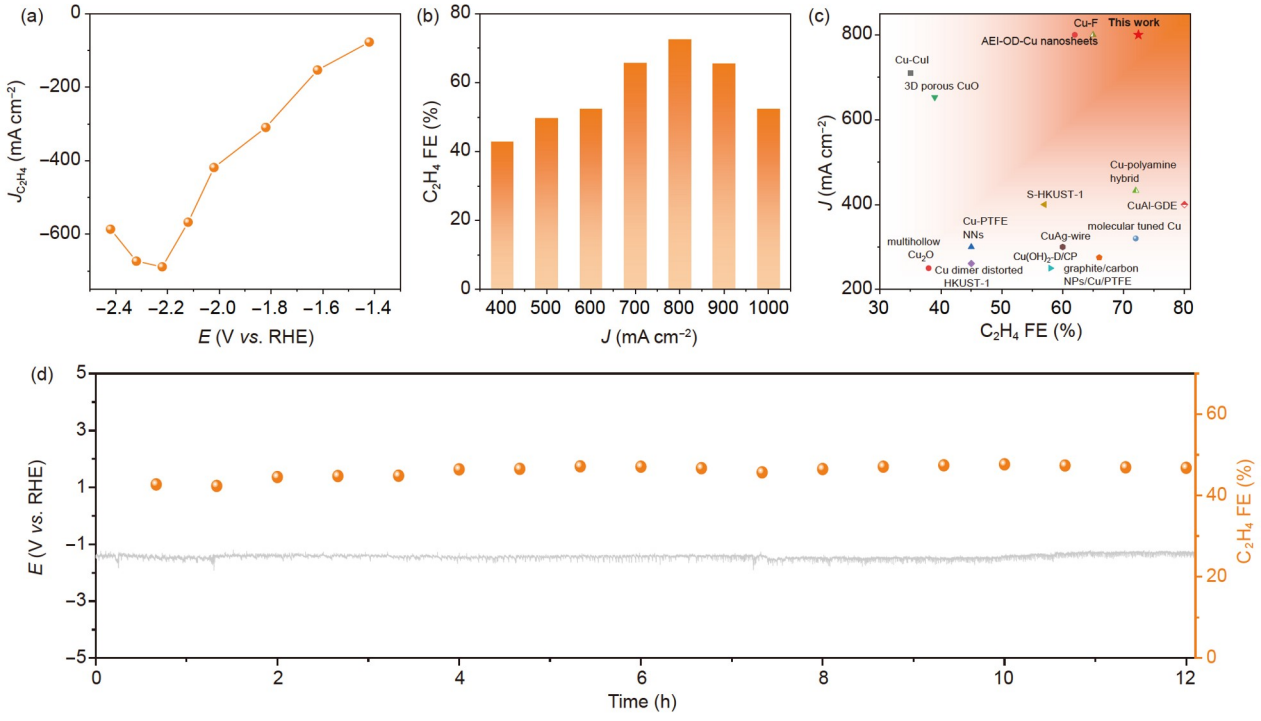

Figure 6 CO_2R performance in a flow cell. (a) Partial current densities of C_2H_4 products over the CuI–CO_2 catalyst under different potentials without *iR* correction. (b) C_2H_4 FEs on CuI–CO_2 under different current densities. (c) Comparison of the CO_2R performance of CuI–CO_2 with that of reported Cu-based catalysts in the flow cell. (d) Stability test of Cu–CO_2 over 12 h in 0.5 mol L^{-1} $KHCO_3$/KI at a current density of 400 mA cm^{-2} (color online).

cells, including Cu–F (65% at 800 mA cm^{-2}), anion exchange ionomer (AEI)–OD–Cu nanosheets (62% at 800 mA cm^{-2}) and molecularly tuned Cu catalysts (72% at 320 mA cm^{-2}) (Figure 6c and Table S8). Apart from the high activity for C_2H_4 production in the flow cell, the CuI–CO_2 electrocatalyst also exhibits outstanding stability at a high current density of 400 mA cm^{-2}, as confirmed by the negligible decay of the potential and C_2H_4 FE over the course of 12 h (Figure 6d). Moreover, the XRD pattern of CuI–CO_2 after this 12-h testing demonstrates the maintenance of CuI (Figure S14), evidencing its robust stability again.

2.5 Mechanism studies by *in-situ* ATR-SEIRS and DFT calculations

To understand the improved CO_2R activity of the CuI–CO_2 nanodots for C_2H_4 generation, we performed *in-situ* ATR-SEIRS analysis (Figure 7 and Figure S15) and DFT calculations (Figure 8) [38–41]. The potential-dependent *in-situ* ATR-SEIRS spectra as shown in Figure 7 and Figure S15 reveal the adsorption of intermediates for C_2H_4 formation over CuI–CO_2, CuI–N_2 and Cu–CO_2 electrocatalysts. Along with negative scanning potentials from −0.1 V to −1.3 V *vs.* RHE, a peak in the 2,068–2,028 cm^{-1} corresponding to adsorbed CO (*CO) becomes visible, accompanied by the progressive emergence of a new shoulder peak due to the reduction of *CO for CuI–CO_2 (Figure 7), suggesting the effective adsorption of *CO intermediates and their rapid reduction. Moreover, the suitable adsorption of *CO enables their rapid dimerization through C–C coupling to form *OCCO species (1,595 cm^{-1}), the key intermediates to generate C_2H_4 [38,41]. Obviously, the peaks of dimerized intermediates *OCCO were detected only on the CuI–CO_2 electrocatalysts compared with CuI–N_2 and Cu–CO_2 electrocatalysts (Figure S15), indicating the greatest preference for the C_2H_4 generation over CuI–CO_2, which agrees with the electrochemical results (Figure 4a–e). Considering that only the peaks of dimerized intermediates of *OCCO were detected on the CuI–CO_2, we believed that the C_2H_4 generation mainly proceeds *via* the *CO dimerization pathways.

DFT calculations were further conducted to gain insights into the positive roles of Cu^+ and CuI(220) facets (Figure 8). The lowest-energy Cu(111) facet and the CuI with (111), (220) and (311) facets were simplified as models for calculations (Figure S16). On the basis of the *in-situ* ATR-SEIRS results, the reduction steps of CO_2 to C_2H_4 on both Cu(111) and CuI(220) start with the hydrogenation of the adsorbed *CO_2 to form *COOH, followed by the OH desorption to generate *CO. Then, two *CO molecules dimerize to *OCCO, which is finally reduced to C_2H_4. *CO dimerization to *OCCO is traditionally considered as the rate-limiting step of CO_2 reduction to C_{2+} [14,20,25]. As displayed in Figure 8a, the Gibbs free energy change (ΔG_{*OCCO}) for the *CO dimerization step over both Cu(111) and CuI(220) is most energy-positive. The ΔG_{*OCCO} over CuI(220) is only 1.4 eV uphill, much lower than that over the Cu(111) slab (1.8 eV).

Interestingly, the ΔG_{*OCCO} over other facts of CuI, including CuI(111) and CuI(311), with respective values of 1.76 and 1.65 eV uphill (Figure 8b), is also lower than that for Cu(111). These comparisons conclusively accentuate that CuI(220) is most favorable for *CO dimerization among the four facets (Figure 8d–g). Moreover, the CuI(220) facet shows stronger affinity with *OCCO intermediates to ac-

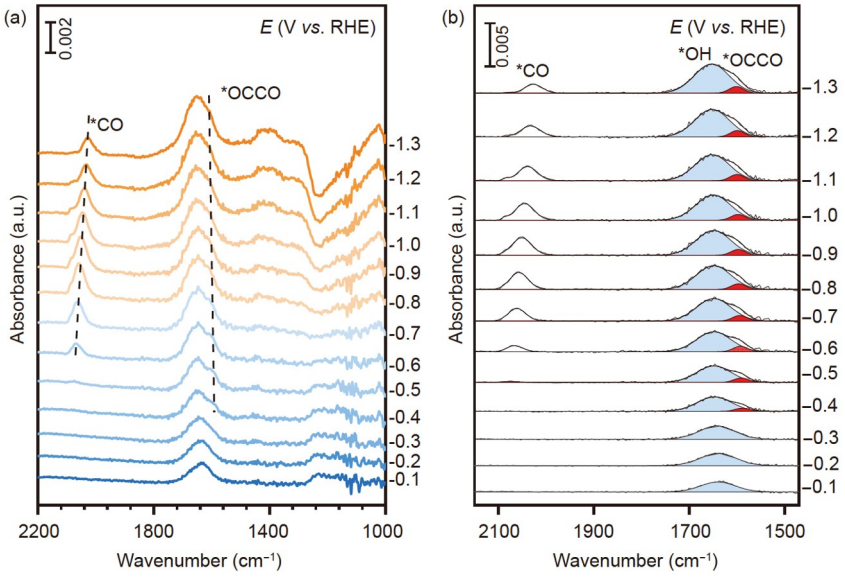

Figure 7 (a) *In-situ* ATR-SEIRS spectra on the surface of the CuI–CO_2 catalyst in 0.1 mol L^{-1} $KHCO_3$/KI electrolyte during negative potential scanning and (b) spectra of the *OH and *OCCO intermediates adsorbed on the CuI–CO_2 catalyst fitted with Gaussian functions (color online).

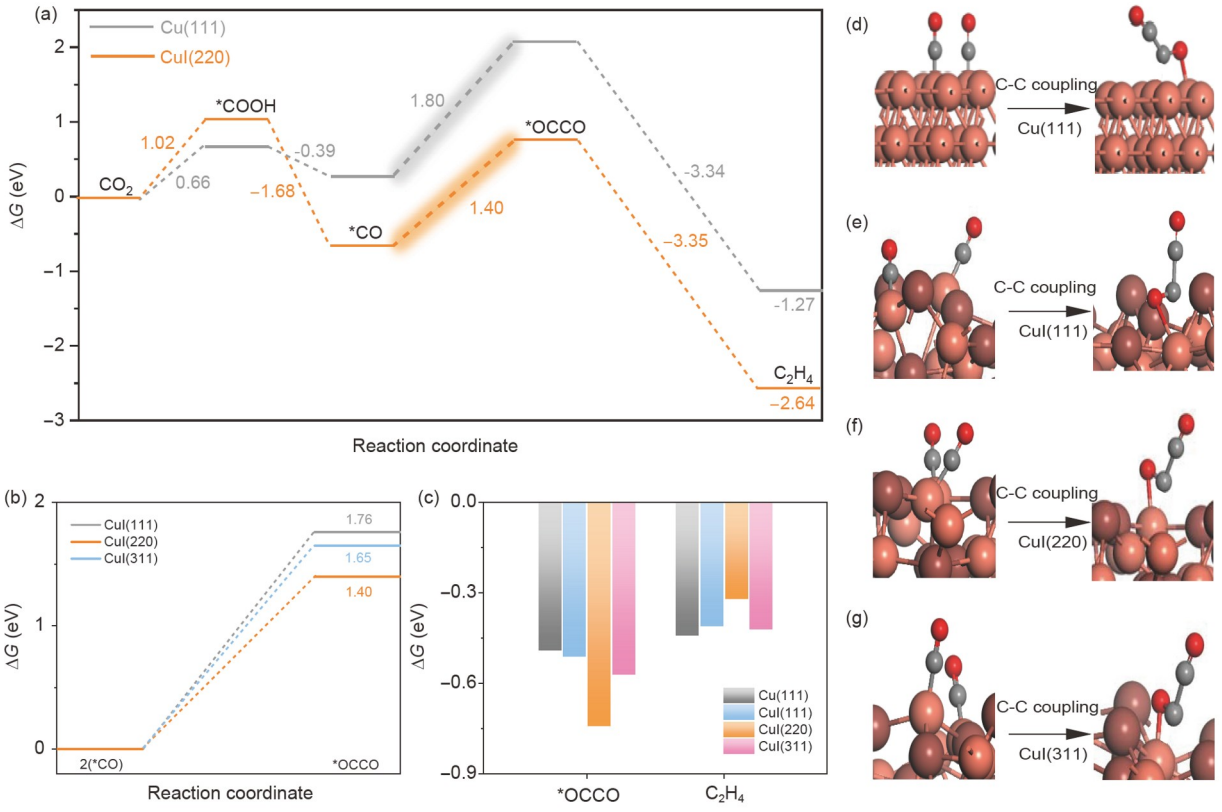

Figure 8 DFT calculation results. (a) Gibbs free energy diagram for CO_2R to C_2H_4 on Cu(111) and CuI(220) facets *via* a direct *CO dimerization pathway. (b) Gibbs free energy changes of *CO dimerization to *OCCO intermediate on CuI(111), CuI(220), and CuI(311) facets. (c) Gibbs free energy changes of key substrate molecules and intermediates that affect the selectivity on Cu(111), CuI(111), CuI(220), and CuI(311) facets. (d–g) Configurations of *CO dimerization to *OCCO intermediate on Cu(111), CuI(111), CuI(220), and CuI(311) facets (color online).

celerate their subsequent hydrogenation and more moderate repellency to C_2H_4 for the following desorption compared with Cu(111), CuI(111) and CuI(311) (Figure 8c). In other words, these DFT calculations certainly demonstrate that the CuI–CO_2 nanodots with favorable (220) facets and a stable Cu^+ state promote selective CO_2 reduction to C_2H_4, which supports our electrochemical and *in-situ* ATR-SEIRS experimental results.

3 Conclusions

In summary, we demonstrate the facile synthesis of cuprous iodide (CuI) nanodots with favorable (220) facets and a stable Cu^+ state for selective CO_2 reduction to C_2H_4 by *operando* reconstruction of $Cu(OH)_2$ in CO_2- and I^--containing electrolytes. The high thermodynamic potential of Cu^{2+}/CuI relative to $Cu^{2+}/Cu^+(Cu^0)$ favors the reduction of Cu^{2+} to Cu^+ of CuI rather than metallic Cu^0, as revealed by X-ray absorption spectroscopy and *in-situ* Raman spectroscopy investigations. DFT calculations and vacuum CO gas adsorption electroresponse testing confirm that CO_2-related intermediates can function as capping agents to facilitate the exposure of CuI(220) facets. The small size of nanodots enables the adequate contact with I^-, which guarantees the rapid formation of CuI instead of the electroreduction to Cu^0. Collectively, the resulting electrocatalyst exhibits a high C_2H_4 Faradaic efficiency of 72.4% at a large current density of 800 mA cm^{-2} and long-term stability. ATR-SEIRS and density functional theory results indicate that the (220) facets and stable Cu^+ synergistically facilitate CO_2/*CO adsorption and *CO dimerization for improved C_2H_4 generation.

Acknowledgements This work is financially supported by The National Key Research and Development Program of China (2021YFA1600800), the Start-up Funding of the Huazhong University of Science and Technology (HUST), the Program for HUST Academic Frontier Youth Team, the National Natural Science Foundation of China (22075092), the National 1000 Young Talents Program of China and The Innovation and Talent Recruitment Base of New Energy Chemistry and Device (B21003).

Conflict of interest The authors declare no conflict of interest.

Supporting information The supporting information is available online at chem.scichina.com and link.springer.com/journal/11426. The supporting materials are published as submitted, without typesetting or editing. The responsibility for scientific accuracy and content remains entirely with the authors.

1 Nitopi S, Bertheussen E, Scott SB, Liu X, Engstfeld AK, Horch S, Seger B, Stephens IEL, Chan K, Hahn C, Nørskov JK, Jaramillo TF, Chorkendorff I. *Chem Rev*, 2019, 119: 7610–7672
2 Liu M, Pang Y, Zhang B, De Luna P, Voznyy O, Xu J, Zheng X, Dinh CT, Fan F, Cao C, de Arquer FPG, Safaei TS, Mepham A, Klinkova A, Kumacheva E, Filleter T, Sinton D, Kelley SO, Sargent EH. *Nature*, 2016, 537: 382–386
3 De Luna P, Hahn C, Higgins D, Jaffer SA, Jaramillo TF, Sargent EH. *Science*, 2019, 364: eaav3506
4 Wang H, Liang Z, Tang M, Chen G, Li Y, Chen W, Lin D, Zhang Z, Zhou G, Li J, Lu Z, Chan K, Tan T, Cui Y. *Joule*, 2019, 3: 1927–1936
5 Li F, Thevenon A, Rosas-Hernández A, Wang Z, Li Y, Gabardo CM, Ozden A, Dinh CT, Li J, Wang Y, Edwards JP, Xu Y, McCallum C, Tao L, Liang ZQ, Luo M, Wang X, Li H, O'Brien CP, Tan CS, Nam DH, Quintero-Bermudez R, Zhuang TT, Li YC, Han Z, Britt RD, Sinton D, Agapie T, Peters JC, Sargent EH. *Nature*, 2020, 577: 509–513
6 Wang G. *Sci China Chem*, 2020, 63: 1023–1024
7 Ji Y, Zheng G. *Sci China Chem*, 2021, 64: 1111–1112
8 Wei Z. *Sci China Chem*, 2022, 65: 421–422
9 Zhong M, Tran K, Min Y, Wang C, Wang Z, Dinh CT, De Luna P, Yu Z, Rasouli AS, Brodersen P, Sun S, Voznyy O, Tan CS, Askerka M, Che F, Liu M, Seifitokaldani A, Pang Y, Lo SC, Ip A, Ulissi Z, Sargent EH. *Nature*, 2020, 581: 178–183
10 Zheng Y, Vasileff A, Zhou X, Jiao Y, Jaroniec M, Qiao SZ. *J Am Chem Soc*, 2019, 141: 7646–7659
11 De Luna P, Quintero-Bermudez R, Dinh CT, Ross MB, Bushuyev OS, Todorović P, Regier T, Kelley SO, Yang P, Sargent EH. *Nat Catal*, 2018, 1: 103–110
12 Wang X, Wang Z, de Arquer FPG, Dinh CT, Ozden A, Li YC, Nam DH, Li J, Liu YS, Wicks J, Chen Z, Chi M, Chen B, Wang Y, Tam J, Howe JY, Proppe A, Todorović P, Li F, Zhuang TT, Gabardo CM, Kirmani AR, McCallum C, Hung SF, Lum Y, Luo M, Min Y, Xu A, O'Brien CP, Stephen B, Sun B, Ip AH, Richter LJ, Kelley SO, Sinton D, Sargent EH. *Nat Energy*, 2018, 5: 478–486
13 Morales-Guio CG, Cave ER, Nitopi SA, Feaster JT, Wang L, Kuhl KP, Jackson A, Johnson NC, Abram DN, Hatsukade T, Hahn C, Jaramillo TF. *Nat Catal*, 2018, 1: 764–771
14 Ma W, Xie S, Liu T, Fan Q, Ye J, Sun F, Jiang Z, Zhang Q, Cheng J, Wang Y. *Nat Catal*, 2020, 3: 478–487
15 Li CW, Kanan MW. *J Am Chem Soc*, 2012, 134: 7231–7234
16 Ren D, Deng Y, Handoko AD, Chen CS, Malkhandi S, Yeo BS. *ACS Catal*, 2015, 5: 2814–2821
17 Chou TC, Chang CC, Yu HL, Yu WY, Dong CL, Velasco-Vélez JJ, Chuang CH, Chen LC, Lee JF, Chen JM, Wu HL. *J Am Chem Soc*, 2020, 142: 2857–2867
18 Zhang G, Zhao ZJ, Cheng D, Li H, Yu J, Wang Q, Gao H, Guo J, Wang H, Ozin GA, Wang T, Gong J. *Nat Commun*, 2021, 12: 5745
19 Wang Y, Wang Z, Dinh CT, Li J, Ozden A, Kibria MG, Seifitokaldani A, Tan CS, Gabardo CM, Luo M, Zhou H, Li F, Lum Y, McCallum C, Xu Y, Liu M, Proppe A, Johnston A, Todorovic P, Zhuang TT, Sinton D, Kelley SO, Sargent EH. *Nat Catal*, 2020, 3: 98–106
20 Zhong D, Zhao ZJ, Zhao Q, Cheng D, Liu B, Zhang G, Deng W, Dong H, Zhang L, Li J, Li J, Gong J. *Angew Chem Int Ed*, 2021, 60: 4879–4885
21 Zhou Y, Che F, Liu M, Zou C, Liang Z, De Luna P, Yuan H, Li J, Wang Z, Xie H, Li H, Chen P, Bladt E, Quintero-Bermudez R, Sham TK, Bals S, Hofkens J, Sinton D, Chen G, Sargent EH. *Nat Chem*, 2018, 10: 974–980
22 Guo C, Guo Y, Shi Y, Lan X, Wang Y, Yu Y, Zhang B. *Angew Chem Int Ed*, 2022, 61: e202205909
23 Zhang W, Huang C, Xiao Q, Yu L, Shuai L, An P, Zhang J, Qiu M, Ren Z, Yu Y. *J Am Chem Soc*, 2020, 142: 11417–11427
24 Wu ZZ, Gao FY, Gao MR. *Energy Environ Sci*, 2021, 14: 1121–1139
25 Zhou X, Shan J, Chen L, Xia BY, Ling T, Duan J, Jiao Y, Zheng Y, Qiao SZ. *J Am Chem Soc*, 2022, 144: 2079–2084
26 Yang R, Duan J, Dong P, Wen Q, Wu M, Liu Y, Liu Y, Li H, Zhai T. *Angew Chem Int Ed*, 2022, 61: e202116706
27 Xiao H, Goddard Iii WA, Cheng T, Liu Y. *Proc Natl Acad Sci USA*, 2017, 114: 6685–6688
28 Yang PP, Zhang XL, Gao FY, Zheng YR, Niu ZZ, Yu X, Liu R, Wu ZZ, Qin S, Chi LP, Duan Y, Ma T, Zheng XS, Zhu JF, Wang HJ, Gao MR, Yu SH. *J Am Chem Soc*, 2020, 142: 6400–6408
29 Jung H, Lee SY, Lee CW, Cho MK, Won DH, Kim C, Oh HS, Min BK, Hwang YJ. *J Am Chem Soc*, 2019, 141: 4624–4633
30 Vasileff A, Zhu Y, Zhi X, Zhao Y, Ge L, Chen HM, Zheng Y, Qiao SZ. *Angew Chem Int Ed*, 2020, 59: 19649–19653
31 Varela AS, Ju W, Reier T, Strasser P. *ACS Catal*, 2016, 6: 2136–2144
32 Xu L, Ma X, Wu L, Tan X, Song X, Zhu Q, Chen C, Qian Q, Liu Z, Sun X, Liu S, Han B. *Angew Chem Int Ed*, 2022, 61: e202210375
33 Yoon A, Poon J, Grosse P, Chee SW, Cuenya BR. *J Mater Chem A*, 2022, 10: 14041–14050
34 Bratsch SG. *J Phys Chem Reference Data*, 1989, 18: 1–21
35 Yuan T, Wang T, Zhang G, Deng W, Cheng D, Gao H, Zhao J, Yu J, Zhang P, Gong J. *Chem Sci*, 2022, 13: 8117–8123
36 Niu ZZ, Chi LP, Liu R, Chen Z, Gao MR. *Energy Environ Sci*, 2021, 14: 4169–4176
37 Kim JY, Zhu P, Chen FY, Wu ZY, Cullen DA, Wang H. *Nat Catal*, 2022, 5: 288–299
38 Kim Y, Park S, Shin SJ, Choi W, Min BK, Kim H, Kim W, Hwang YJ. *Energy Environ Sci*, 2020, 13: 4301–4311
39 Pérez-Gallent E, Figueiredo MC, Calle-Vallejo F, Koper MTM. *Angew Chem Int Ed*, 2017, 56: 3621–3624
40 Zhu S, Jiang B, Cai WB, Shao M. *J Am Chem Soc*, 2017, 139: 15664–15667
41 Deng B, Huang M, Li K, Zhao X, Geng Q, Chen S, Xie H, Dong X, Wang H, Dong F. *Angew Chem Int Ed*, 2022, 61: e202114080